Understanding the Capacitive Charge in Bulk Porous Electrodes by Mathematical Modeling

Qingzhen Yang,[1,2,3,4] Xinmiao Jia,[1,2] Xiangming Li,[3,*] Qingxi Yang,[5] Tingting Zhang,[6] Xiankun Huang,[7] Qinwen Zheng,[3] Congming Li,[3] and Jinyou Shao[3]

[1] *The Key Laboratory of Biomedical Information Engineering of Ministry of Education, School of Life Science and Technology, Xi'an Jiaotong University, Xi'an, Shaanxi 710049, People's Republic of China*

[2] *Bioinspired Engineering and Biomechanics Center (BEBC), Xi'an Jiaotong University, Xi'an, Shaanxi 710049, People's Republic of China*

[3] *Micro-/Nano-Technology Research Center, State Key Laboratory for Manufacturing Systems Engineering, Xi'an Jiaotong University, Xi'an, Shaanxi 710049, People's Republic of China*

[4] *Research Institute of Xi'an Jiaotong University, Hangzhou, Zhejiang 311215, People's Republic of China*

[5] *Army Engineering University, Shijiazhuang Campus, Shijiazhuang, Hebei 050003, People's Republic of China*

[6] *College of Mechanical and Electrical Engineering, Shaanxi University of Science and Technology, Xi'an, Shaanxi 710021, People's Republic of China*

[7] *School of Chemical Engineering and Technology, Xi'an Jiaotong University, Xi'an, Shaanxi 710049, People's Republic of China*

(Received 28 November 2021; accepted 28 March 2022; published 22 April 2022)

Supercapacitors exhibit immense potential in electric vehicles and national grids due to their high power density. The power and energy density of supercapacitors largely depend on the design of electrodes and the composition of electrolytes, which dominate the capacitive charging process. However, the availability of only a few mathematical models for capacitive charging in bulk porous electrodes has limited the rational design of a supercapacitor in practice. Herein, a mathematical model is proposed to predict the charging process in a porous electrode and is then experimentally validated. In this model, the dependence of capacitive behavior on the conductivity of both the electrode and electrolyte, as well as the porosity and thickness of electrode, are systematically discussed. Moreover, different charging modes, e.g., potentiostatic charging, potentiodynamic charging, and galvanostatic charging, are studied. The results of this model indicate that the conductivity of the electrolyte (even though it is an aqueous electrolyte) is the bottleneck that limits the charging rate of a supercapacitor, in particular, in thick electrode films. This mathematical model could be a powerful tool for optimizing the design of both electrodes and electrolytes for high-performance supercapacitors.

DOI: 10.1103/PhysRevApplied.17.044045

I. INTRODUCTION

Portable electronics (e.g., mobile phones) and electric vehicles (EVs) have widespread applications in various fields, making great demands for mobile power supplies. To date, various types of energy-storage techniques have been developed based on capacitors, supercapacitors, batteries, or fuel cells. For EVs, a supercapacitor is considered as a promising mobile power supply and has attracted significant research attention due to its numerous advantages, such as high power density (rapid charging-discharging, as high as approximately 10 kW kg^{-1}) and light weight [1,2].

A supercapacitor basically consists of two electrodes placed in liquid electrolyte and isolated from an electrical contact by a semipermeable membrane acting as a separator. A supercapacitor is charged by applying an external voltage on the two electrodes. Subsequently, ions from the electrolyte are attracted toward the porous electrodes and eventually get absorbed on the surface of the electrode. At the interface between a porous electrode and electrolyte, charges from the electrode and ions from the electrolyte together form the electric double layer. The essence of charging a supercapacitor is to store charge (including electronic and ionic charges) inside the porous electrodes. The amount of charge is closely dependent on the surface area; therefore, porous electrodes with a high surface area are favorable for developing efficient supercapacitors [3]. Carbon materials, e.g., graphene, carbon nanotubes, and activated carbon (AC), act as excellent candidates for electrodes, due to their high porosity, light weight, and acceptable conductivity [4–6].

*xiangmingli@mail.xjtu.edu.cn

In general, supercapacitors require high-performance electrodes and electrolytes. To date, significant research efforts have been devoted to improving the performance of supercapacitors with respect to charging rate and energy density [7,8]. Researchers have developed various electrode materials with high conductivity and a large mass-surface area ratio, including carbon materials, metallic oxides, and polymers. The capacitor has been improved to the scale of as high as about kF g^{-1} or kF cm^{-3}. Moreover, different electrolytes, ranging from aqueous electrolytes to nonaqueous electrolytes, and from liquid electrolytes to solid electrolytes, are used in supercapacitors. For the commonly used aqueous electrolytes, the limiting cell voltage is about 1.5 V. At a higher voltage, water electrolysis occurs. In contrast, nonaqueous electrolytes can bear a higher cell voltage of about 3 V [6,9,10].

However, the performance of supercapacitors depends not only on the physical properties of electrolytes and electrodes, but also on the match between them. For a given electrolyte, the thickness and porosity of the electrode need to be delicately designed for optimization of the supercapacitor's performance. Design optimization relies on an understanding of the capacitive charge in bulk porous electrodes. Some researchers conducted a theoretical study to better comprehend the charging mechanism of supercapacitors. They report that the theoretical models can basically be divided into two categories, i.e., the microscopic model and the macroscopic model. By using a microscopic model, the formation process of an electric double layer is investigated [11–16]. In general, the domain of the model lies at the micro- or nanoscale (usually 1 to 100 nm) and the structure of the electrode consists of one or a few holes. The methods for the microscopic models include molecular simulation methods [11–14], the Poisson-Nernst-Planck model [15,17], and the Poisson-Boltzmann model [18,19]. A microscopic model can provide detailed information on the charging process, and the sizes of ions and holes can be fully considered [20,21]. The major disadvantage of microscopic models is that they are computationally demanding. The size of a supercapacitor is usually on a scale of centimeters or even larger and includes numerous holes in the electrodes; thus, it is difficult to use microscopic models to simulate the charging process at the device level.

In contrast, a macroscopic model is based on the theory of classical electrodynamics and is able to predict the function of supercapacitors at the device level [22–26]. For instance, Posey and Morozumi modeled a metal electrode with a single hole and solved the electric potential and charge distribution [27]. Notably, porous electrode theory is usually adopted in macroscopic models. A porous electrode is characterized by the accessible area and the apparent conductivity. The charging process can be described by using differential equations. However, it is difficult to analytically solve the governing equations. Therefore, some simplifications are frequently made, e.g., the conductivity of the electrode is much higher than that of the electrolyte and the charging current is kept constant (galvanostatic charging mode). Using the abovementioned simplifications, Srinivasan and Weidner modeled the charging process of electric-double-layer capacitors [28]. The differential equations are transferred to the Laplace domain and analytical solutions are proposed for the equations. Popov *et al.* calculated the charging process of supercapacitors by considering the chemical reaction [29–31]. For other cases (potentiostatic and potentiodynamic charging modes), the governing equations do not provide any solution. For the general cases, a numerical scheme is required to solve the equations.

Another alternative to model supercapacitors is the transmission-line (TL or equivalent circuit) model [32]. It is based on an infinite succession of electrode slices connected together. Each slice is described by a capacitor and a resistor. To simplify the analysis, the TL model divides the entire supercapacitor into some slices. The key point is how to determine the capacitance and resistance. If they are determined by using the Poisson-Nernst-Planck equation, then the TL method yields to the microscopic model. Alternatively, if these parameters are predicted by using the porous electrode theory, the model becomes the macroscopic one. The number of slices in the TL model determines the accuracy of the model. In the two-slice TL model, the charge of the supercapacitor can be solved analytically [33]. However, a more accurate solution needs more slices and is difficult to solve analytically. Although significant progress has been made in modeling electric-double-layer supercapacitors, a comprehensive numerical model that can simulate the charging process and charge distribution inside the porous bulk electrode and electrolytes is still lacking.

Here, a macroscopic mathematical model is developed to predict the performance of supercapacitors. The governing equations are actually the same as those mentioned in the previous literature studies. However, these equations are difficult to solve analytically, and thus, a numerical scheme is proposed to solve them. The electric potentials in the electrode and electrolyte are coupled together and are solved simultaneously with appropriate boundary conditions. The model can be employed to unveil the charging process and the distribution of charge inside the electrodes. Compared with other models, the model proposed in this study enables galvanostatic, potentiostatic, and potentiodynamic charging modes. The conductivities of the porous electrode, confined electrolyte, and bulk electrolyte are all considered. Notably, most macroscopic porous electrode models consider only the galvanostatic charging mode and ignore the resistance of the porous electrode and bulk electrolyte. Additionally, the present model can provide abundant information, including the potential, current, and charges on both sides (porous electrode and electrolyte).

Most macroscopic porous electrode models enable the calculation of the potential difference between the electrode and electrolyte. However, information on the bulk electrolyte is usually not considered. By using this model, the influence of the following parameters, i.e., conductivity and porosity of the electrode, conductivity of the electrolyte, charging mode (e.g., potentiostatic charging, potentiodynamic charging, and galvanostatic charging), is systematically investigated. Besides, a supercapacitor is fabricated and its performance is compared with the numerical results, which validate the numerical model. The present mathematical model could be of great help and guiding significance to design high-performance supercapacitors.

II. MATHEMATICAL FORMULATION

A. Problem statement

A typical supercapacitor is illustrated in Fig. 1(a). A pair of porous electrodes are placed in a face-to-face manner, and the electrodes and separator between them are filled with electrolyte throughout. In general, a layer of metal is bound on the outer side of each electrode, which is referred to as the current collector. The positive and negative electrodes are assumed to be of the same material with the same thickness, L_0, and at a separating distance of L_1. The width and length of the supercapacitor are much larger than the thickness; thus, the problem can be simplified into the one-dimensional (1D) case. All the physical parameters are functions of x.

The electrode is composed of two phases, i.e., the porous matrix and the surrounding electrolyte. The conductivity of the porous matrix is denoted by σ_m. In the separator, the conductivity of the bulk electrolyte is its intrinsic value, σ_{s0}. In the confined electrolyte in electrodes, the apparent conductivity is represented by σ_s (usually $\sigma_s < \sigma_{s0}$ due to porosity). When charging, an external voltage, U, is imposed upon the current collectors, and the value of U can be a constant or it may vary with time. Furthermore, current is generated in the porous matrix, confined electrolyte, and bulk electrolyte. The current density is denoted by j_m, j_s, and j_{s0}, correspondingly. The electric double layer is formed in the porous electrode, and the storage charge density is q with a total amount of Q_t.

B. Governing equations

The model is based on porous electrode theory. It is effective when the microscopic features are much smaller than the system's dimensions, which allows for juxtaposing and volume averaging of the liquid and solid phases in forming a continuum set of equations. Herein, in the experimental setup, the electrodes are made of AC. The pore sizes are in the order of nanometers and the breadth of the carbon particles is in the order of a few microns; thus, the porous electrode theory can effectively describe the system. The computational domain includes two regions, i.e., the porous electrode, Ω_1, and the bulk electrolyte, Ω_2. For these two regions, the governing equations are different, and thus, discussed separately. The porous electrode consists of two components, i.e., the porous matrix and the surrounding electrolyte. The voltage drop across the matrix-electrolyte interface is defined as follows:

$$\Delta\phi = \phi_m - \phi_s \quad \in \Omega_1, \tag{1}$$

where ϕ_m is the electric potential of the porous matrix and ϕ_s is that of the confined electrolyte, and Ω_1 denotes the domain of the electrode [Fig. 1(b)]. According to Ohm's law, the current density in the matrix and confined electrolyte can be expressed as follows:

$$j_m = -\sigma_m \frac{\partial \phi_m}{\partial x} \quad \in \Omega_1, \tag{2}$$

$$j_s = -\sigma_s \frac{\partial \phi_s}{\partial x} \quad \in \Omega_1, \tag{3}$$

where σ_m and σ_s are the effective conductivities. Moreover, charge distributes in the matrix and electrolyte with

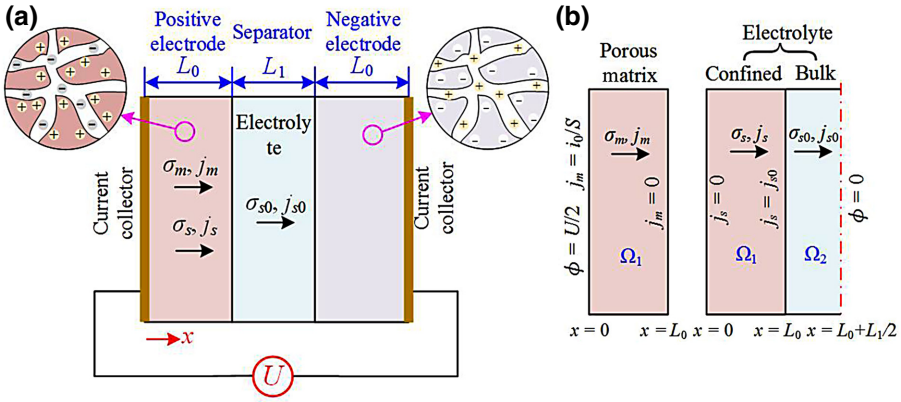

FIG. 1. A typical supercapacitor with porous electrodes: (a) Configuration and (b) computational domain, where Ω_1 and Ω_2 represent the domains of the electrode and separator, respectively.

densities q_m and q_s, respectively:

$$\frac{\partial q_m}{\partial t} = -\frac{\partial j_m}{\partial x} \quad \in \Omega_1, \tag{4}$$

$$\frac{\partial q_s}{\partial t} = -\frac{\partial j_s}{\partial x} \quad \in \Omega_1. \tag{5}$$

Herein, it is assumed that all the charge distributes on the interface, and the surface area of unit volume (specific interfacial area) of the porous electrode is A. The surface charge density can be expressed as follows:

$$\rho_m = \frac{q_m}{A} \quad \in \Omega_1, \tag{6}$$

$$\rho_s = \frac{q_s}{A} \quad \in \Omega_1. \tag{7}$$

In general, equivalent amounts of charges with opposite signs are accumulated on the two sides of electric double layer:

$$\rho_m = -\rho_s \quad \in \Omega_1. \tag{8}$$

The capacity per unit area (specific differential capacitance) of the electric double layer is denoted by C_d, which can be expressed as the ratio between the surface charge density and voltage difference

$$C_d = \frac{\rho_m}{\Delta\phi} = \frac{\partial \rho_m/\partial t}{\partial(\phi_m - \phi_s)/\partial t} \quad \in \Omega_1. \tag{9}$$

In this study, it is assumed that C_d is constant during the charging process. By combining the abovementioned equations, we have

$$\begin{aligned} \frac{\partial^2 \phi_m}{\partial x^2} &= \frac{AC_d}{\sigma_m}\frac{\partial(\phi_m - \phi_s)}{\partial t} \quad \in \Omega_1, \\ \frac{\partial^2 \phi_s}{\partial x^2} &= -\frac{AC_d}{\sigma_s}\frac{\partial(\phi_m - \phi_s)}{\partial t} \quad \in \Omega_1, \end{aligned} \tag{10}$$

Equation (10) describes the spatial-temporal evolution of electric potentials ϕ_m and ϕ_s in the porous electrode, and the two potentials, ϕ_m and ϕ_s, are coupled together. If the potentials are solved, the current and surface charge density can be obtained. For the bulk electrolyte, there is no net charge. Thus, the governing equation is

$$\frac{\partial \rho_s}{\partial t} = -\frac{\partial j_{s0}}{\partial x} = \sigma_{s0}\frac{\partial^2 \phi_{s0}}{\partial x^2} = 0 \quad \in \Omega_2, \tag{11}$$

where σ_{s0} represents the conductivity of the bulk electrolyte (usually $\sigma_{s0} > \sigma_s$), ϕ_{s0} is the electric potential, and Ω_2 is the domain of the bulk electrolyte.

C. Boundary conditions

The configuration is symmetric with respect to the middle plane ($x = L_0 + L_1/2$), only half of the domain is computed for simplification [Fig. 1(b)]. To enable the solution of governing Eqs. (10) and (11), some boundary conditions and initial conditions are required. Boundary and initial conditions could be different for different cases. In the following study, the general boundary and initial conditions are listed. If different conditions are used, they are indicated hereafter. In the electrode, the initial condition is represented as follows:

$$\phi_m = \phi_s = 0 \quad \in \Omega_1 \times (t = 0), \tag{12}$$

where t denotes the time. Moreover, the potential in the bulk electrolyte is also zero:

$$\phi_{s0} = 0 \quad \in \Omega_2 \times (t = 0). \tag{13}$$

At the left boundary of the electrode, the current density of the electrolyte is zero and that of the porous matrix is determined by the inflow current density:

$$j_s = -\sigma_s\frac{\partial \phi_s}{\partial x} = 0 \quad \in \{\partial\Omega_1 | x = 0\} \times (0, t), \tag{14}$$

$$j_m = -\sigma_m\frac{\partial \phi_m}{\partial x} = j_0 \quad \in \{\partial\Omega_1 | x = 0\} \times (0, t), \tag{15}$$

where j_0 is the current flux that flows into the supercapacitor. The electric potential of the porous matrix is specified as follows:

$$\phi_m = U/2 \quad \in \{\partial\Omega_1 | x = 0\} \times (0, t), \tag{16}$$

where U is the imposed external voltage. At the right boundary of the electrode, the current density of the porous matrix is zero:

$$j_m = -\sigma_m\frac{\partial \phi_m}{\partial x} = 0 \quad \in \{\partial\Omega_1 | x = L_0\} \times (0, t). \tag{17}$$

In the domain of the bulk electrolyte, the electric potential at the middle plane is assumed to be zero, which is considered to be the reference potential:

$$\phi_{s0} = 0 \quad \in \{\partial\Omega_2 | x = L_0 + L_1/2\} \times (0, t). \tag{18}$$

At the interface of the electrode and bulk electrolyte, the potential and current are continuous:

$$\sigma_s\frac{\partial \phi_s}{\partial x} = \sigma_{s0}\frac{\partial \phi_{s0}}{\partial x} \quad \in \{\Omega_1 \cap \Omega_2 | x = L_0\} \times (0, t), \tag{19}$$

$$\phi_s = \phi_{s0} \quad \in \{\Omega_1 \cap \Omega_2 | x = L_0\} \times (0, t). \tag{20}$$

For Eqs. (15) and (16), usually one of j_0 and U is specified during the charging process. For potentiostatic and potentiodynamic charging, the external voltage, U, is known. For galvanostatic charging, the current flux, j_0, is specified.

D. Computational method

Governing Eqs. (10) and (11) are discretized and solved numerically along with appropriate boundary conditions. The equations are discretized by using a simple implicit finite-difference scheme [34]. After discretization, the equations become

$$\frac{\phi_{m,i+1}^{t+\Delta t}+\phi_{m,i-1}^{t+\Delta t}-2\phi_{m,i}^{t+\Delta t}}{\Delta x^2} = \frac{AC_d}{\sigma_m}\left(\frac{\phi_{m,i}^{t+\Delta t}-\phi_{s,i}^{t+\Delta t}}{\Delta t}-\frac{\phi_{m,i}^{t}-\phi_{s,i}^{t}}{\Delta t}\right),$$
$$\frac{\phi_{s,i+1}^{t+\Delta t}+\phi_{s,i-1}^{t+\Delta t}-2\phi_{s,i}^{t+\Delta t}}{\Delta x^2} = \frac{AC_d}{\sigma_s}\left(\frac{\phi_{s,i}^{t+\Delta t}-\phi_{m,i}^{t+\Delta t}}{\Delta t}-\frac{\phi_{s,i}^{t}-\phi_{m,i}^{t}}{\Delta t}\right),$$
$$\frac{\phi_{s0,i+1}^{t+\Delta t}+\phi_{s0,i-1}^{t+\Delta t}-2\phi_{s0,i}^{t+\Delta t}}{\Delta x^2}=0, \tag{21}$$

where Δx is the grid step, subscript i denotes the ith nodal point in the x direction, superscript t indicates the variable at time t, and Δt is the time step. For the boundary conditions, there are some first-order terms that are discretized by the central difference scheme. Considering Eq. (15) as an example, the discretized form is

$$\frac{\phi_{m,2}^{t+\Delta t}-\phi_{m,0}^{t+\Delta t}}{2\Delta x}=-\frac{j_0}{\sigma_m}. \tag{22}$$

The other boundary conditions can be discretized in the same manner.

By performing the discretization over each nodal point and then assembling, the final equations can be obtained in the following form:

$$M\mathbf{X}=\mathbf{F}, \tag{23}$$

where M is the global stiffness matrix, $\mathbf{X}=[\phi_{m,1}^{t+\Delta t},\ldots,\phi_{m,N_0}^{t+\Delta t},\phi_{s,1}^{t+\Delta t},\ldots,\phi_{s,N_0}^{t+\Delta t},\phi_{s0,1}^{t+\Delta t},\ldots,\phi_{s0,N_1}^{t+\Delta t},j_0,U]^T$ is the unknown vector, and $\mathbf{F}$ is the force vector. With the initial conditions, Eq. (23) can be solved in a time-marching manner and the unknowns at different times can be obtained. After obtaining ϕ_m, ϕ_s, and ϕ_{s0}, the charge densities q_m and q_s can be solved. More details of the numerical scheme are described in the Appendix.

III. EXPERIMENT

To validate the numerical model, an AC-based supercapacitor [Fig. 2(a)] is fabricated and some experimental tests are performed. The AC films are prepared as follows: polyvinylidene difluoride (PVDF, HSV900, Arkema, 0.5 g) is first dissolved in N-methyl pyrrolidone (NMP, >99%, Aladdin, 120 ml) to form a homogeneous solution by stirring for 3 h in a glovebox. AC (YEC-8B, 8.0 g) and carbon black (BP2000, Cabot, 1.5 g) are mixed by magnetic stirring and then dried at 120 °C for 10 h. The carbon mixture is added to the PVDF solution in an agate jar, followed by milling for 24 h, which affords a well-dispersed AC slurry. The carbon slurry is then coated on aluminum foil (22 μm thick, AFT Electronic Co., Ltd., Guangdong, China) *via* doctor blading, followed by baking at 60 °C for 12 h in a glovebox to evaporate the NMP solvent, which results in the formation of an AC film

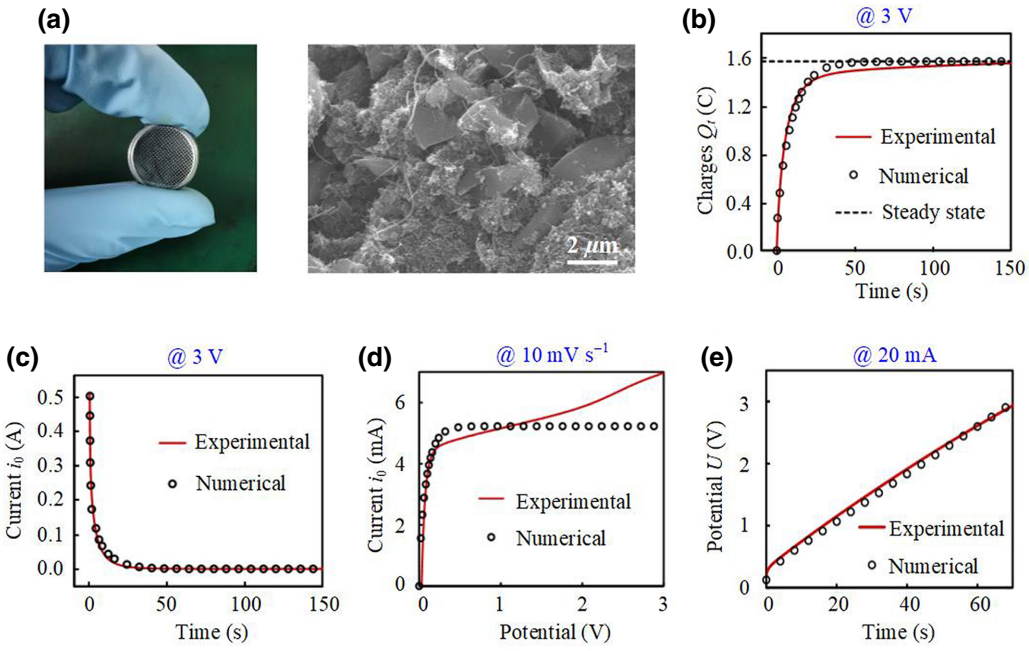

FIG. 2. Experimental validation of the model. (a) Fabricated supercapacitor and SEM image of the porous electrode structure. (b) Stored charge, Q_t, and (c) current, i_0, in potentiostatic charging mode. (d) Current-potential (C-V) curve of the supercapacitor in potentiodynamic charging mode. (e) Potential of supercapacitor U in galvanostatic charging mode.

with an aluminum current collector. The scanning electron microscopy (SEM) image of AC is obtained using a scanning electron microscope (Hitachi SU8010). The AC electrode film is then soaked in electrolyte [1 mol l^{-1} ammonium tetrafluoroborate in propylene carbonate (Et_4NBF_4/PC)] overnight for good infiltration of electrolyte. The AC film is punched into small pieces and then symmetrically assembled with a separator layer made of Celgard film.

The supercapacitor has a button-cell-like shape with a diameter of $D = 1.2$ cm. The material of the porous electrode is AC with a thickness of $L_0 = 120$ μm. The distance between two electrodes, i.e., the size of the separator, is $L_1 = 260$ μm. The electrolyte used is Et_4NBF_4/PC with a concentration of 1 mol l^{-1}. The supercapacitor is charged on an electrochemical working station (Versastat 3, Princeton Applied Research, USA) at room temperature. Different modes, e.g., potentiostatic, potentiodynamic, and galvanostatic, are selected. The charging voltage and current are recorded. The stored charge is obtained by integrating the current over time.

IV. RESULTS

A. Comparison with experimental results

Numerical simulations are performed and compared against experimental results. Prior to that, the values of some parameters are required. According to the mathematical model, variables such as the conductivity of the porous matrix, σ_m; the conductivity of the confined electrolyte, σ_s; the conductivity of the bulk electrolyte, σ_{s0}; the porosity of the electrode (specific interfacial area), A; and the specific differential capacitance of the electric double layer, C_d, may affect the performance of supercapacitors. The conductivity of the porous electrode is $\sigma_m = 100$ S m^{-1}, which is measured using a four-point-probe resistance tester (Zhuhai Kaivo Optoelectronic Technology Co., Ltd.) The porosity, i.e., specific interfacial area, of the electrode can be measured by N_2-adsorption analysis or predicted by using density-functional theory calculations. Different methods result in different values of porosity, ranging from 1.9×10^9 to 2.6×10^9 m^2 m^{-3} (or m^{-1}) [35]. In the present study, it is assumed that $A = 2.3 \times 10^9$ m^{-1}.

Furthermore, the specific differential capacitance, C_d, is derived from experimental results. The supercapacitor is charged in potentiostatic mode with $U = 3$ V. The stored charges achieve a steady state of $Q_t = 1.57$ C [Fig. 2(a)]. Theoretically, the total charge at steady state is expressed as $Q_t = C_d A U L_0 S/2$, where C_d is the specific differential capacitance, A is the porosity, U is the imposed voltage, L_0 is the thickness of the porous electrode, and S is the cross-section area of the button-cell supercapacitor. In this manner, we can obtain $C_d = 0.033$ F m^{-2}. Actually, C_d is a variable that depends on some parameters, such as the materials of the electrode and electrolyte, the concentration of the electrode, the porosity of the electrode, and voltage [36]. For a given supercapacitor, most of the abovementioned parameters are fixed, and the porosity of the electrode can be considered as uniform. Then, the differential capacity, C_d, depends only on the voltage. Different models, such as the Helmholtz model, the Gouy-Chapman model, and the Gouy-Chapman-Stern model, are proposed to describe the relationship between differential capacitance and voltage [36]. For simplification, the Helmholtz model, with constant differential capacitance, is employed in the present study.

The bulk conductivity of the electrolyte is assumed to be $\sigma_{s0} = 1.3$ S m^{-1} [37]. For the apparent conductivity of a confined electrolyte, σ_s, some nuclear magnetic resonance spectroscopy experiments reveal that it is reduced by 2 orders of magnitude with respect to the bulk conductivity, σ_{s0} [38]. In this study, this value is obtained by correlation with experimental results. When $\sigma_s = 0.05$ S m^{-1}, the numerical simulation fits best with experiments [Fig. 2(a)]. With these values specified, the charging process for supercapacitors can be obtained.

Furthermore, herein, the performance of the supercapacitor is tested for different charging modes. In potentiostatic charging, a step voltage of $U = 3$ V is imposed on the current collectors and the charging current, i_0, is monitored. For comparative analysis, the experimental results together with numerical simulations are both shown in Fig. 2(b). The experimental and numerical results are consistent with each other. The stored charge, Q_t, is calculated by integrating the current [Fig. 2(b)]. The charge increases gradually until it reaches steady state (i.e., saturation state). Moreover, the current is also depicted in Fig. 2(c). The current is large at the beginning and then decays gradually. Eventually, the current decreases to zero. In potentiodynamic charging, the applied voltage, U, increases with a scan rate of 10 mV s^{-1} until 3 V. Figure 2(d) illustrates that the experimental results and numerical ones are consistent at a low voltage; however, the discrepancy appears at a high voltage. One possible reason is the occurrence of spurious Faradaic reactions at high voltage. Finally, galvanostatic charging with a constant current of $i_0 = 20$ mA is performed. In this case, the potential increases linearly with time [Fig. 2(e)]. These results indicate that the numerical model can predict the performance of supercapacitors and the results are consistent with experimental results.

B. Potentiostatic charging

After validating the numerical model, it is used with confidence to simulate the charging process in different modes. In potentiostatic charging mode, the imposed potential, U, is fixed as a constant [Fig. 1(a)]. Without losing generality, the voltage is selected to be $U = 1$ V. Herein, the size of the separator is changed to $L_1 = 160$ μm. Actually, the results obtained from the numerical model

are in one dimension (the x direction). For a better illustration, the 1D simulation results are extended into a two-dimensional (2D) representation. Taking advantage of symmetry, the obtained results are mirrored to the entire supercapacitor. Equation (8) indicates that the electrodes are electrically neutral, i.e., equivalent charges with opposite signs are accumulated in the porous matrix and in the confined electrolyte. Figure 3(a) illustrates the charge density during the charging process. A positive (negative) value indicates that the charge in the porous matrix is positive (negative). The charge is zero at the beginning due to the initial condition. The charge starts to appear at the electrode-electrolyte interface ($t = 1$ s). As time is prolonged, more charge emerges inside the electrode ($t = 5$ s). At $t = 10$ s, a considerably large amount of charge is accumulated in the electrodes. The charge is still nonuniform, i.e., the density at the electrode-electrolyte interface is higher than that deep inside. Eventually, the charge achieves its saturation state and the distribution becomes spatially uniform ($t = 50$ s). The arrows in Fig. 3(a) indicate the motion of negative charges in the electrolyte.

Moreover, the profiles of ϕ_m and ϕ_s along the x direction in the positive electrode are plotted [Figs. 3(b) and 3(c)]. For the potential of porous matrix ϕ_m, the required time to achieve its equilibrium state is significantly shorter. This can be attributed to the fact that the conductivity of the electrode (porous matrix) is much higher than that of the confined electrolyte, $\sigma_m \gg \sigma_s$, and the potential in the electrode achieves the equilibrium state instantly when the voltage is imposed. Figure 3(b) illustrates that the matrix becomes an equal-potential body for $t = 10^{-3}$ s, and the corresponding potential equals that of the current collector, $U/2 = 0.5$ V. The potential of the electrolyte, ϕ_s, can be divided into two parts, namely, confined electrolyte in the electrode and the bulk electrolyte. In the bulk electrolyte, ϕ_s is fixed as zero [Fig. 3(c)]. In the confined electrolyte, $\phi_s = 0.5$ V at the beginning ($t = 0.1$ s). As time is prolonged, it decreases gradually and eventually reaches the equilibrium state, $\phi_s = 0$ ($t = 50$ s). At the equilibrium state, the potential difference is $\phi_m - \phi_s = 0.5$ V over the entire electrode.

To reveal the evolution of ϕ_s, ϕ_s at $x = 0$ is monitored [Fig. 3(d)]. It is 0.5 V at the beginning and then gradually decreases to zero ($t = 50$ s). When a different voltage is imposed ($U = 2$ and 3 V), a similar trend is observed. The charge density, q_m, is found to be proportional to $\phi_m - \phi_s$, and the profile is shown in Fig. 3(e). The figure reveals that the charge starts to emerge at the electrode-electrolyte interface and then appears inside the electrode. At equilibrium state (i.e., steady state), the charge density is spatially uniform and the saturation value is $q_m = C_d AU/2 = 38.5$ C cm^{-3}. For charge accumulation, the required time $t = 50$ s is on the same scale of potential in electrolyte ϕ_s. Furthermore, the stored charge in total is also calculated, and the results are shown in Fig. 3(f). The total charge, Q_m, increases gradually and the equilibrium value is proportional to the imposed voltage U. Comparative analysis of the total charge with different voltages ($U = 1$, 2, and 3 V) indicates that a higher voltage leads to more charge in the electrode. For $U = 1$ V, the equilibrium value is $Q_m = C_d AUL_0/2 = 0.462$ C m^{-2} (in the positive electrode). One important issue of supercapacitor charging is the efficiency. In this study, time t_c is used to characterize the efficiency, which indicates the time that is required to charge 63% of the saturation value. When $U = 1$ V, the required time is $t_c = 7.5$ s.

Equations (4) and (5) indicate that the charge originates from the current. Therefore, the profiles of the current in the porous matrix, in the electrolyte, and that in the current collector are plotted in Figs. 3(g)–3(i), respectively. In the porous matrix, the current j_m is large near the collector ($x = 0$) and decreases to zero at $x = L_0$. For temporal evolution, the current decays with time. In the electrolyte, the current j_s also decreases with time. For the spatial distribution, it is zero at $x = 0$ and then increases gradually until $x = L_0$. In the bulk electrode, the current is constant along the x direction. The current through collector j_0 is essentially equal to j_m at $x = 0$. Figure 3(i) illustrates that j_0 decreases dramatically with time until it becomes zero. During potentiostatic charging, the imposed voltage, U, is a step function. There are steady states for the current, charge density, and total charge. At steady state, the current is zero, the charge density is $q_m = C_d AU/2$, and the total charge is $Q_m = C_d AUL_0/2$.

C. Potentiodynamic charging

In potentiodynamic charging, the imposed voltage, rather than being constant, is a temporally varied value. In this section, the linearly increased voltage $U = \alpha t$, where α is a constant and t is the time, is discussed. It is assumed that the charging process is terminated when $U = 1$ V. Figure 4(a) depicts the temporal-spatial evolution of stored charge, q_m, with $\alpha = 20$ mV s^{-1}. The charge density is zero initially. Once the potential is imposed, charge starts to appear at the electrode-electrolyte interface, and the density decreases toward the current collector. At $t = 50$ s, a significant amount of charge is accumulated in the electrodes.

For potentiodynamic charging, the potential of the porous electrode, ϕ_m, approximately equals U, which increases linearly with time. The voltage linearly increases and reaches 1 V after 50 s. The potential of the electrolyte, ϕ_s, is recorded during the charging process, and the profile along the x direction is plotted, as shown in Fig. 4(b). In potentiodynamic charging mode, ϕ_s is initially zero and then increases gradually. The potential in the bulk electrolyte; however, remains zero all the time. To better illustrate the evolution of ϕ_s, its value at $x = 0$ is monitored [Fig. 4(c)]. When $\alpha = 20$ mV s^{-1}, $\phi_s(x = 0)$ increases

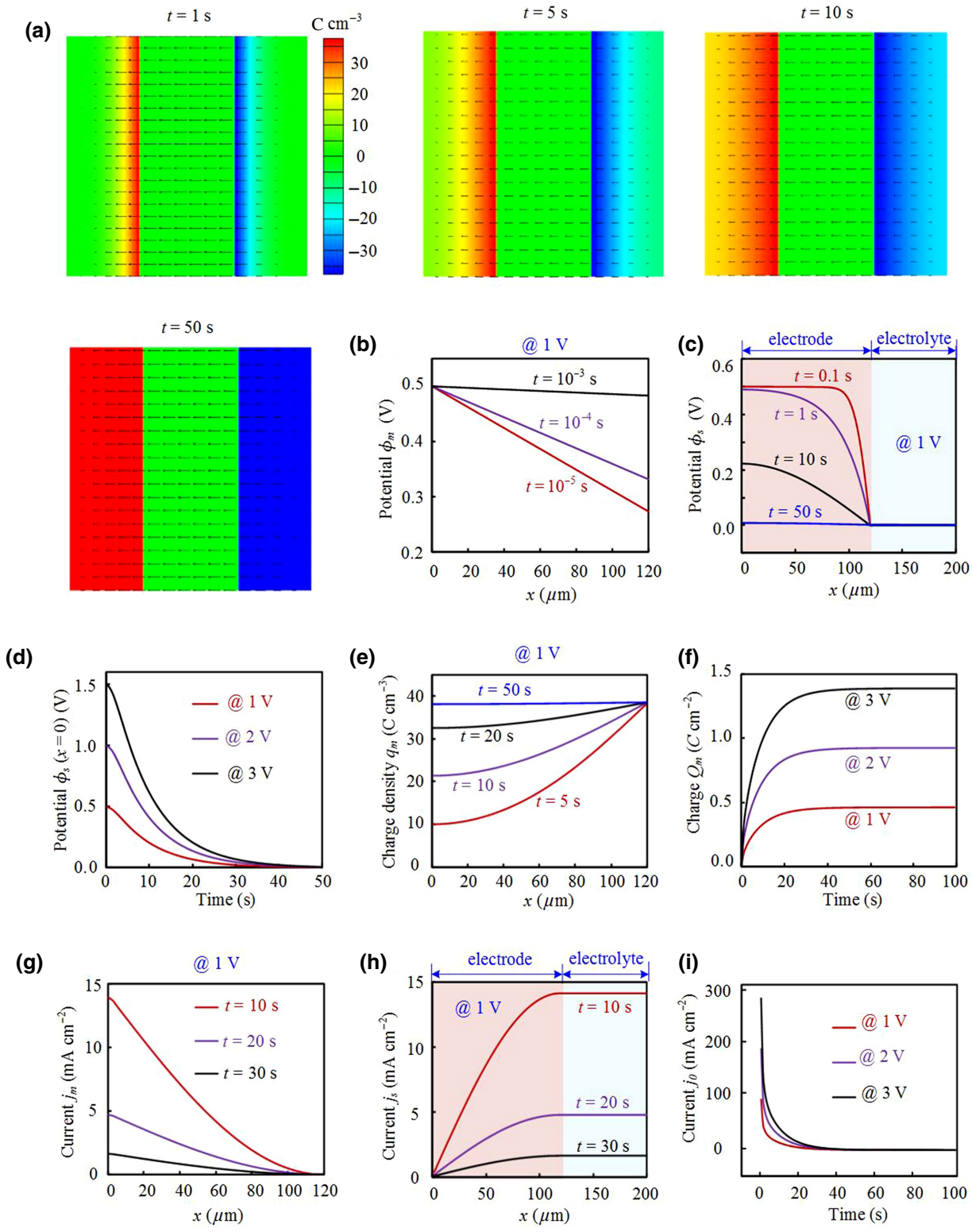

FIG. 3. Charging process in potentiostatic mode. (a) Spatial distribution of stored charge, q_m, at $t = 1$, 5, 10, and 50 s. For a better illustration, results are extended to the entire supercapacitor according to symmetry. (b) Profiles of ϕ_m along the x direction. (c) Profiles of ϕ_s along the x direction. (d) Evolution of ϕ_s at $x = 0$ for different charging voltages, $U = 1$, 2, and 3 V. (e) Profiles of charge density, q_m, along the x direction. (f) Total charge, Q_m, in the domain (one electrode) at different voltages. (g) Profiles of current in porous matrix j_m along the x direction. (h) Profiles of current in electrolyte j_s along the x direction. (i) Charging current flux j_0.

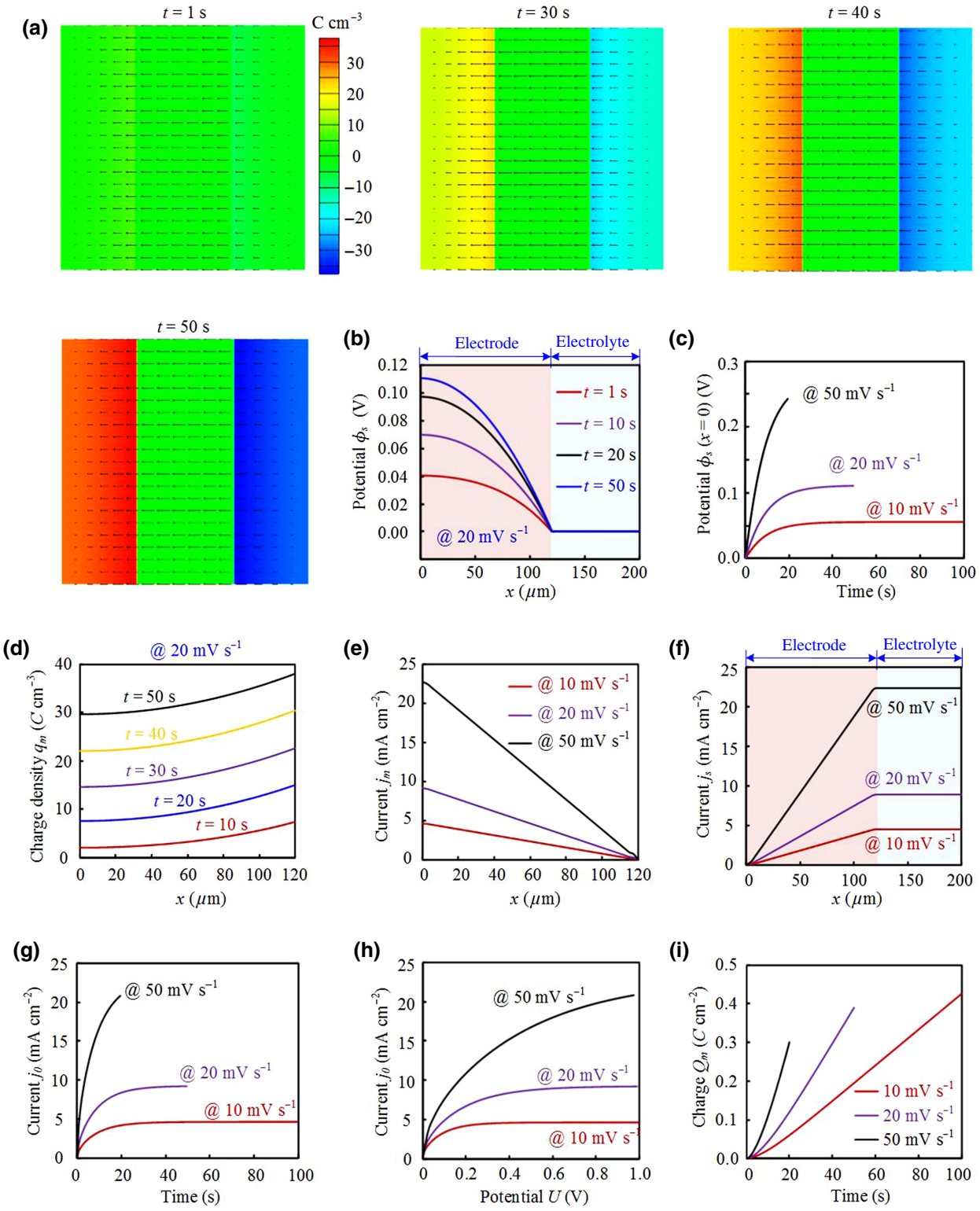

FIG. 4. Charging process in potentiodynamic mode. (a) Spatial distribution of stored charge, q_m, at $t = 1$, 30, 40, and 50 s, with scan rate $\alpha = 20$ mV s^{-1}. (b) Profiles of ϕ_s along the x direction. (c) Evolution of $\phi_m(x = 0)$ for different scan rates $\alpha = 10$, 20, and 50 mV s^{-1}. (d) Profiles of q_m along the x direction at different times. (e) Profiles of current in the porous matrix, j_m, along the x direction. (f) Profiles of current in the electrolyte, j_s, along the x direction. (g) Current in the current collector, j_0. (h) Relationship between potential and current (C-V curve). (i) Total charge, Q_m, in the domain (one electrode) at different scan rates.

rapidly at the beginning and then increases slowly. At $t = 50$ s, the imposed voltage is $U = 1$ V. $\phi_s(x = 0)$ at this time arrives at its steady state at 0.11 V. When $\alpha = 10$ mV s^{-1}, the evolution of $\phi_s(x = 0)$ is similar and its steady value is 0.056 V. For $\alpha = 50$ mV s^{-1}, $\phi_s(x = 0)$ has not yet arrived at its steady state when the charging process is terminated at $t = 20$ s.

Moreover, the charge density, q_m, is higher at the electrode-electrolyte interface and is lower near the current collector ($x = 0$). As the time is prolonged, the charge density increases [Fig. 4(d)]. When the charging process is terminated at $t = 50$ s, the maximum value of q_m is 38.5 C cm^{-3}, which equals the saturation value in potentiostatic charging mode. Furthermore, the current in the porous matrix and electrolyte is monitored herein. Figures 4(e) and 4(f) exhibit plots of the profiles of current at the termination time, that is, $t = 100$ s for $\alpha = 10$ mV s^{-1}; $t = 50$ s for $\alpha = 20$ mV s^{-1}, and $t = 20$ s for $\alpha = 50$ mV s^{-1}. As illustrated, a larger α leads to a higher current. For a given α, j_m is higher near the collector and decreases to zero when getting away from collector. Current j_s is zero at the collector and increases to a large value with x. In the bulk electrolyte, the value of j_s is a constant along the x direction.

The current in collector j_0 is initially zero and then gradually increases to the steady state [Fig. 4(g)]. A larger α leads to a higher current j_0. When $\alpha = 50$ mV s^{-1}, current j_0 does not become steady when the charging process is terminated at $t = 20$ s. Figure 4(h) shows a plot of current j_0 as the function of applied voltage, which is commonly referred to as a *C-V* curve. For a given potential U, the corresponding current j_0 is higher for a larger α. Notably, the curve of $\alpha = 50$ mV s^{-1} does not become flat when $U = 1$ V. As mentioned in the previous section, the total charge, Q_m, is calculated and plotted in Fig. 4(i). For a higher α, the charge increases more rapidly. Nevertheless, the charging time is short; therefore, the stored total charge is still less than the case with a small α. In potentiodynamic charging mode, the potential in the electrolyte and the current in the collector exhibit steady states. The potential in the collector and the stored charge tend to increase continuously with time.

D. Galvanostatic charging

Galvanostatic charging is another strategy for charging supercapacitors. In this mode, current j_0 is fixed as a constant. Figure 5(a) depicts the spatial distribution of charge during galvanostatic charging with a current of $j_0 = 10$ mA cm^{-2}. Initially, the charge is zero and then accumulates gradually. When $t = 20$ and 30 s, the charge is nonuniform. The density is higher at the electrode-electrolyte interface and is lower near the collector. At $t = 40$ s, the potential, U, increases to 1 V. During the charging process, the potential, ϕ_s, is monitored and the profiles are plotted in Fig. 5(b). The potential, ϕ_s, is zero at the beginning and increases with time. After $t = 10$ s, ϕ_s achieves its steady state and does not change with time. To better illustrate the evolution of ϕ_s, its value at $x = 0$ is recorded [Fig. 5(c)]. For different currents, j_0, ϕ_s achieves its steady state after $t = 10$ s, and the steady value is proportional to current j_0. For $j_0 = 5$, 10, and 20 mA cm^{-2}, the steady values of $\phi_s(x = 0)$ are 0.06, 0.12, and 0.24 V correspondingly.

Furthermore, the profiles of charge density, q_m, at different times are plotted in Fig. 5(d). As the time is prolonged, the charge density, q_m, increases gradually. Along the x direction, q_m is higher near the electrode-electrolyte interface and is lower at the collector side. For the current in the porous matrix, j_m, it is approximately a linearly decreased function along the x direction [Fig. 5(e)]. Moreover, the value of j_m is proportional to the charging current j_0. Different from j_m, the current in the electrolyte increases with x and it becomes a constant in the bulk electrolyte. Figures 5(e) and 5(f) demonstrate that the current profiles at the termination time, that is, $t = 85$, 40, and 17 s correspond to $j_0 = 5$, 10, and 20 mA cm^{-2}. At the termination time, the potential, U, is 1 V.

Figure 5(g) exhibits a plot of the potential, U, as a function of time. The figure illustrates that U increases gradually until 1 V and the scan rate is higher for a large charging current, j_0. As shown in the previous section, the total charge, Q_m, is calculated. Figure 5(h) exhibits a plot of Q_m as a function of potential, U, showing that more charge is stored for a small charging current, j_0. In galvanostatic charging mode, potential ϕ_s and currents j_m and j_s achieve steady states. However, potential U, charge density q_m, and total charge Q_m increase continuously with time, i.e., there is no steady state.

E. The effect of other parameters

For an ideal supercapacitor, the target is high power density and high energy density. During the charging process, the challenging task is how to store more charge in a shorter time. Conductivity is a key factor that affects the charging speed. Moreover, a higher conductivity leads to a faster charging speed. In experiments, some parameters, e.g., porosity and conductivity, are related. In this study, however, when changing one parameter, the others are kept fixed. The main objective is to ease the analysis of the influence of each parameter. For a supercapacitor, usually, the conductivity of a confined electrolyte, σ_s, is smaller compared with those of the porous matrix and bulk electrolyte. Thus, σ_s becomes the bottleneck that limits the charging speed. Figure 6(a) shows a comparative analysis of the total charge, Q_m, with different σ_s. The charging mode is selected as potentiostatic charging with $U = 1$ V. For $\sigma_s = 0.025$, 0.05, and 0.1 S m^{-1}, the saturated charge is the same. However, the charging speed is higher

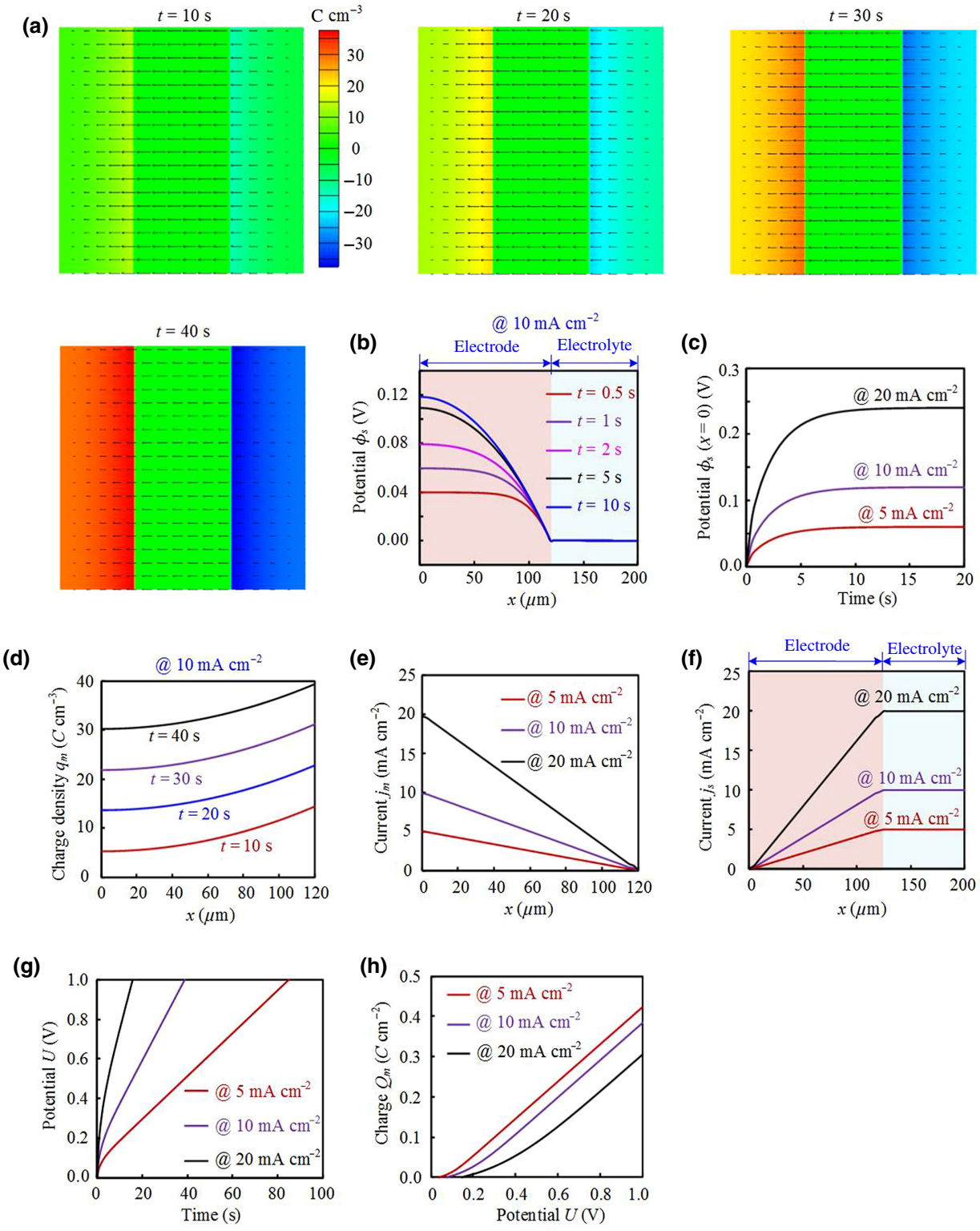

FIG. 5. Charging process in galvanostatic mode. (a) Spatial distribution of stored charge, q_m, at $t = 10$, 20, 30, and 40 s, with charging current $j_0 = 10$ mA cm^{-2}. (b) Profiles of ϕ_s along the x direction at different times. (c) Potential ϕ_s at $x = 0$ for different charging currents $j_0 = 5$, 10, and 20 mA cm^{-2}. (d) Profiles of charge density, q_m, along the x direction. (e) Profile of current j_m. (f) Profile of current j_s. (g) Development of potential U for different current fluxes j_0. (h) Total charge, Q_m, in the domain (one electrode) as functions of applied potential U.

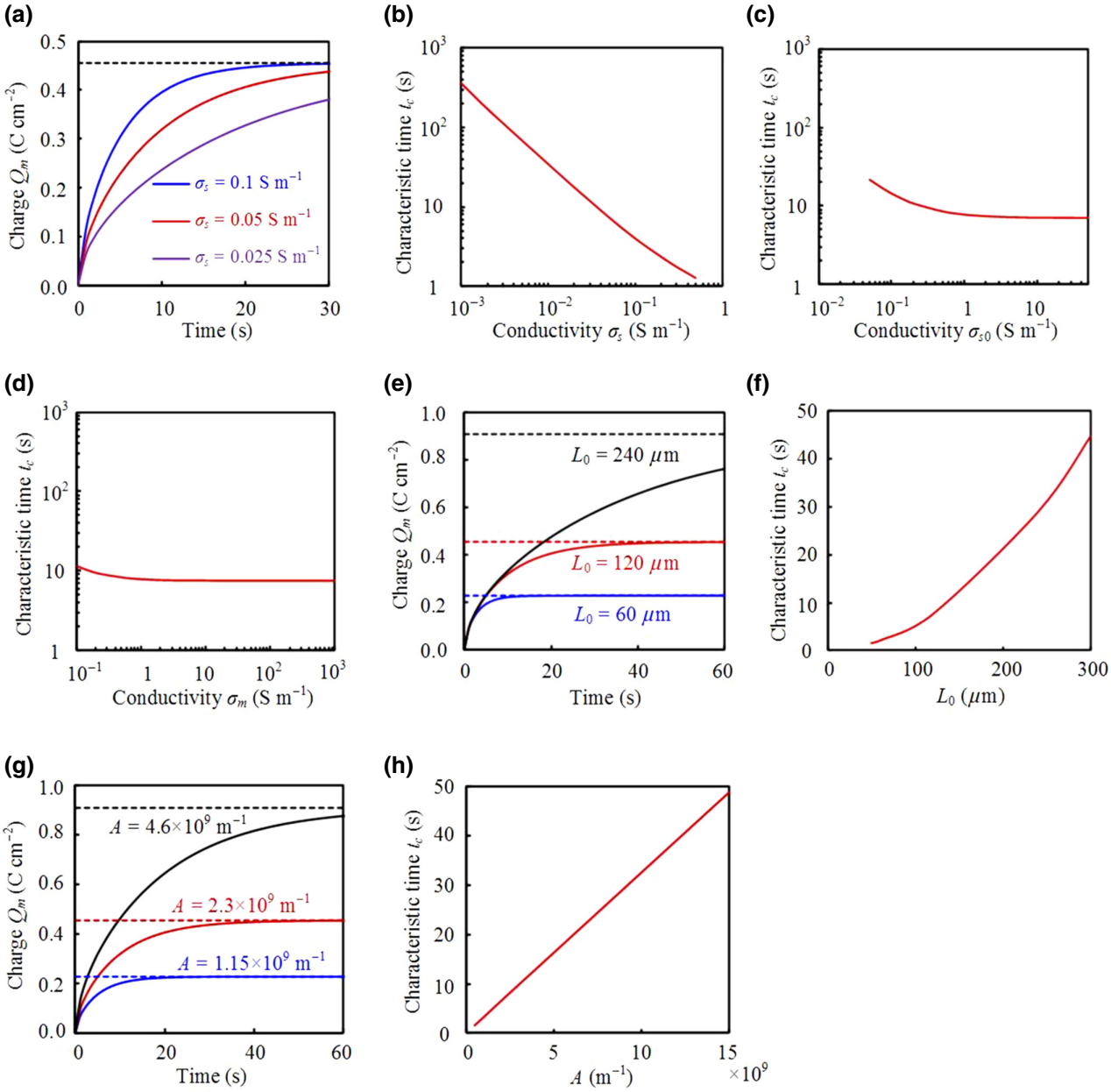

FIG. 6. Effect of parameters on the charging process. (a) Stored charge for different conductivities of the confined electrolyte, σ_s. (b) Relationship between σ_s and characteristic time t_c. (c) Influence of the conductivity of the bulk electrolyte, σ_{s0}, on characteristic time t_c. (d) Influence of the conductivity of the electrode, σ_m, on characteristic time t_c. (e) Stored charge for different electrode breadths, L_0. (f) Influence of electrode breadth L_0 on characteristic time t_c. (g) Stored charge for different specific interfacial areas, A. (h) Influence of specific interfacial area A on characteristic time t_c.

when σ_s is larger, that is, more charge is stored in a short time.

To quantify the charging speed, the characteristic time of the supercapacitor, t_c, which represents the time to achieve 63% saturation charge, is defined. Figure 6(b) depicts the characteristic time of supercapacitor t_c with different conductivities, σ_s. A larger σ_s results in a smaller t_c. If an electrolyte with a higher conductivity (in particular, in the confined phase) can be developed, the charging speed can be significantly improved. The effects of the conductivities of the bulk electrolyte and electrode on the characteristic time, t_c, are shown in Figs. 6(c) and 6(d). The influence is insignificant, unless σ_{s0} (or σ_m) is small. When σ_{s0} (or σ_m) is in the same order as σ_s, it becomes visible, such that characteristic time t_c decreases with σ_{s0} (or σ_m). Furthermore, the impact of the breadth of the porous electrode on the charging process is studied herein. It is known that a thicker electrode can store more charge. However, it

takes a longer time to achieve its steady state [Fig. 6(e)]. For a given thickness L_0, characteristic time t_c is calculated as indicated in Fig. 6(f), revealing that t_c increases proportionally with the thickness of the electrode.

It is known that the porosity of the electrode is a key parameter that affects the performance of a supercapacitor. To date, various methods have been proposed to improve the porosity for a higher energy density [39]. In this study, porosity is characterized by the specific interfacial area (accessible area), A. With an increase of porosity A, more charges are stored in the supercapacitor [Fig. 6(g)]. Moreover, characteristic time t_c is calculated. Figure 6(h) reveals that the characteristic time increases linearly with porosity. The effect of the specific differential capacitance, C_d, on the charging process is similar to that of porosity A. This is attributed to the fact that they appear together as AC_d in governing Eqs. (10).

F. Electrochemical impedance spectroscopy

Electrochemical impedance spectroscopy (EIS) is a helpful tool to characterize the frequency response of a supercapacitor [40–44]. Herein, EIS is conducted on the supercapacitor by using the numerical model. In general, the impedance is measured by imposing a low-amplitude alternating voltage, ΔU, on a steady-state potential, U, with $\Delta U = \Delta U_{\text{amp}} \sin(\omega t)$, where $\omega = 2\pi f$ is the pulsation and f is the frequency. The results of the numerical simulation indicate that impedance spectroscopy is independent of the steady-state potential, U, and the amplitude of ΔU. Without losing generality, we select $U = 0$ and $\Delta U_{\text{amp}} = 1$ V.

For further verification, a voltage of $U = \sin(200\pi t)$, corresponding to an alternating voltage with 100 Hz frequency, is applied to the supercapacitor. The charging current is recorded and illustrated in Fig. 7(a). The open circles are the results obtained from the numerical simulation. Five cycles (i.e., periods) are shown herein, and the results correspond to approximately a sinusoidal function. Next, the results are fitted with a sinusoidal curve, $\Delta j_0 = \Delta j_{\text{amp}} \sin(\omega t + \varphi)$, where φ is the phase angle. The results after curve fitting are denoted by the continuous line in Fig. 7(a). For the first cycle, some discrepancy appears between the open circles and the continuous line. Furthermore, they are consistent with each other. The supercapacitor is charged from the quiescent state, i.e., the potential and charges are zero ($U = 0$, $q = 0$) at $t = 0$. The open circles shown in Fig. 7(a) reveal that the current is zero when $t = 0$, indicating that the phase angle is zero. However, owing to the capacitive reactance, the pace of the current is left behind by the voltage. After a few cycles, the phase angle reaches a steady value. By fitting the curve, a phase angle of $\varphi = 13°$ is obtained, i.e., the continuous line does not pass the point (0, 0). In experiments, the same phenomenon is also observed. When measuring the phase angle in experiments, usually the first or second cycles are abandoned.

In the same manner, herein, the frequency of the imposed voltage is changed and the amplitude of current Δj_{amp} and phase angle φ are calculated. The voltage and current are written in the form of a complex number, $\Delta U = \Delta U_{\text{amp}}\, e^{i\omega t}$ and $\Delta j_0 = \Delta j_{\text{amp}}\, e^{i(\omega t+\varphi)}$. The impedance is defined as $Z(\omega) = \Delta U/\Delta j_0$. It can

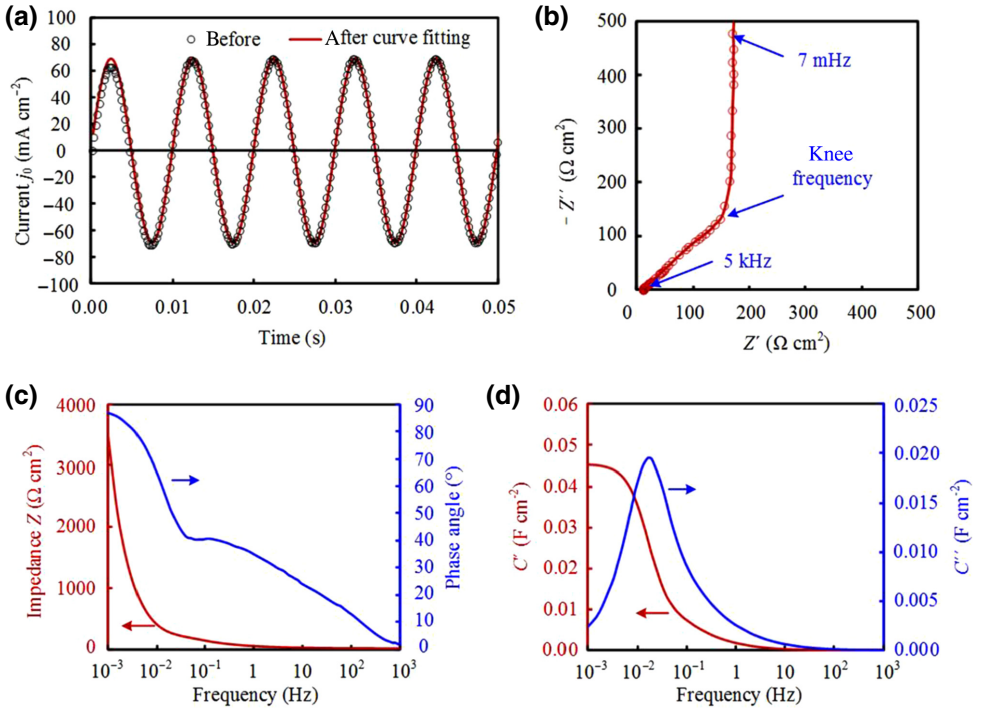

FIG. 7. Impedance spectroscopy by numerical simulation. (a) Evolution of current flux j_0 under 100-Hz charging voltage, $U = \sin(200\pi t)$. Open circles are the results obtained from numerical simulation, and the continuous line is the result of sinusoidal curve fitting. (b) Nyquist plots of impedance. (c) Impedance and phase angle versus frequency plots. (d) Evolution of the real part and imaginary part of capacitance versus frequency.

be written as a complex number, $Z(\omega) = Z'(\omega) + iZ''(\omega)$, where $Z'(\omega)$ and $Z''(\omega)$ are the real part and imaginary part of impedance, respectively [41]. By substituting, we have

$$Z'(\omega) = \frac{\Delta U_{\text{amp}}}{\Delta j_{\text{amp}}} \cos(\varphi), \tag{24}$$

$$Z''(\omega) = -\frac{\Delta U_{\text{amp}}}{\Delta j_{\text{amp}}} \sin(\varphi), \tag{25}$$

$$|Z(\omega)| = \frac{\Delta U_{\text{amp}}}{\Delta j_{\text{amp}}}. \tag{26}$$

These equations can be used to calculate the impedance of a supercapacitor. The relationship between Z' and Z'' is depicted in Fig. 7(b), which is usually referred to as the Nyquist diagram of the impedance. At high frequency, the curve is quite linear. In contrast, at low frequency, the imaginary impedance changes sharply and the curve tends to be a vertical line, that is, the supercapacitor behaves like a resistor. The crossing of this line with the low-frequency vertical line is referred to as the knee frequency, which occurs at about 0.03 Hz. Additionally, the magnitude of impedance, $|Z(\omega)|$, and phase angle, φ, vs the frequency, f, are plotted. Figure 7(c) illustrates that the impedance decreases with frequency. Moreover, the phase angle also decreases with frequency. At $f = 10^{-3}$ Hz, the phase angle approaches 90°. At $f = 10^{3}$ Hz, the phase angle becomes almost 0.

Another parameter to describe the supercapacitor is the complex capacitance modeling of impedance data [40]. The complex capacitance is defined as $C(\omega) = 1/i\omega Z(\omega)$, and it can be written under its complex form $C(\omega) = C'(\omega) - iC''(\omega)$. By substituting, we have

$$C'(\omega) = -\frac{Z''(\omega)}{\omega |Z(\omega)|^2} = \frac{\Delta j_{\text{amp}} \sin(\varphi)}{2\pi f\, \Delta U_{\text{amp}}}, \tag{27}$$

$$C''(\omega) = \frac{Z'(\omega)}{\omega |Z(\omega)|^2} = \frac{\Delta j_{\text{amp}} \cos(\varphi)}{2\pi f\, \Delta U_{\text{amp}}}, \tag{28}$$

$$|C(\omega)| = \frac{\Delta j_{\text{amp}}}{2\pi f\, \Delta U_{\text{amp}}}. \tag{29}$$

For the given parameters, $C'(\omega)$ and $C''(\omega)$ are calculated. Figure 7(d) depicts the evolution of the real part and the imaginary part of capacitance vs frequency. Clearly, the real capacitance, $C'(\omega)$, decreases with frequency. At low frequency, the decrease is significant and the decrease becomes slow with frequency. For the imaginary capacitance, $C''(\omega)$, a peak appears at $f = 0.02$ Hz. When the frequency is higher or lower than this value, the imaginary capacitance decreases.

To explain the results presented in Fig. 7, the TL model is employed (Fig. 8). To date, various TL models have been developed to describe the charging behavior of supercapacitors. The simplest one is the *RC* model, which includes an ideal capacitor, C, and a resistor, R, in series [Fig. 8(a)]. For this case, the corresponding impedance is $R - (1/\omega C)i$. The Nyquist plot is expected to be a vertical line with an intersection point $(R, 0)$ at the x axis, which is inconsistent with that shown in Fig. 7(b). To fix this problem, the TL model is modified by connecting a capacitor, C_1, in parallel with resistor R, and it is assumed that $C_1 \gg C_2$. For this case, the corresponding impedance is $\frac{R}{1+\omega^2 R^2 {C_1}^2} - \left(\frac{\omega R^2 C_1}{1+\omega^2 R^2 {C_1}^2} + \frac{1}{\omega C_2}\right) i$. The real part is $Z'(\omega) = R/(1 + \omega^2 R^2 {C_1}^2)$ and the imaginary part is $Z''(\omega) = -\left(\frac{\omega R^2 C_1}{1+\omega^2 R^2 {C_1}^2} + \frac{1}{\omega C_2}\right)$. Since $C_1 \gg C_2$, $Z''(\omega) \approx -(1/\omega C_2)$, and its magnitude decreases monotonously with the increase of frequency. The real part can be approximated as a constant, $Z'(\omega) \approx R$, when the frequency is low. Thus, the corresponding Nyquist plot is a vertical line because the value on the x axis is constant and the value on the y axis decreases continuously. For a high frequency, the real impedance is $Z'(\omega) = R/(1 + \omega^2 R^2 {C_1}^2)$, which decreases with an increase of frequency. In the Nyquist plot, both values are decreased on the x and y axes. This is consistent with the results shown in Fig. 7(b).

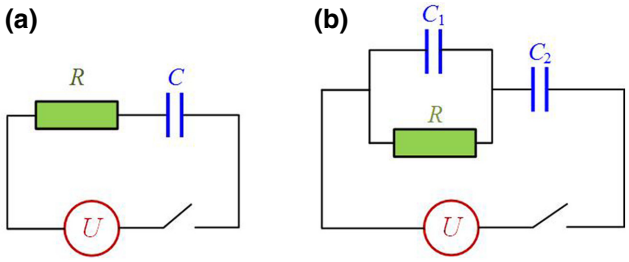

FIG. 8. TL models for the supercapacitor. (a) Simple *RC* model and (b) modified *RC* model.

The modified TL model can be used to explain the results shown in Fig. 7(d). According to Eqs. (27) and (28), the real capacitance is $C'(\omega) = C_2\left(1 - \frac{{C_2}^2}{{C_1}^2 + {C_2}^2 + 1/\omega^2 R^2}\right)$, and the imaginary capacitance is $C''(\omega) = \frac{1}{\omega R({C_1}^2 + {C_2}^2) + 1/\omega R}$. With an increase of frequency, the real capacitance decreases monotonically. However, the imaginary capacitance first increases and then decreases. The peak value is $C''(\omega) = 1/(2\sqrt{{C_1}^2 + {C_2}^2})$ when $\omega = 1/(R\sqrt{{C_1}^2 + {C_2}^2})$. These results are consistent with the results presented in Fig. 7(d).

V. DISCUSSION

As mentioned previously, the supercapacitor system is governed by three coupled equations that are difficult to solve numerically. In this study, an in-house code is developed to enable numerical solutions. For readers without a background in computer programming, it could be difficult to reproduce the abovementioned results. Thus, an attempt

is made herein to develop a simplified numerical model. The main objective is to enable the solution with some commercial software. Thus, readers can solve the model with ease.

To attain this objective, some simplifications are required. Owing to the porosity of the electrode, the conductivity of the confined electrolyte is much smaller than that of the bulk electrolyte, i.e., $\sigma_s \ll \sigma_{s0}$. Moreover, the conductivity of the porous matrix is usually much larger than that of the confined electrolyte, i.e., $\sigma_m \gg \sigma_s$. With these two assumptions, the model can be simplified. The conductivity of the bulk electrolyte is significantly high; therefore, the electric potential can be treated as a constant $\phi_{s0} = 0$, and Eq. (11) becomes redundant. In the same manner, the potential of the porous matrix is also a constant, $\phi_m = U/2$. Equation (10) can be rewritten as follows:

$$\frac{\partial^2(\Delta\phi)}{\partial x^2} = AC\left(\frac{1}{\sigma_m} + \frac{1}{\sigma_s}\right)\frac{\partial(\Delta\phi)}{\partial t} \approx \frac{AC_d}{\sigma_s}\frac{\partial(\Delta\phi)}{\partial t} \quad \in \Omega_1, \tag{30}$$

where $\Delta\phi = \phi_m - \phi_s$. Equation (30) is the governing equation in domain Ω_1, and domain Ω_2 becomes redundant. The initial and boundary conditions can be rewritten as follows:

$$\Delta\phi = 0 \quad \in \Omega_1 \times (t = 0), \tag{31}$$

$$\frac{\partial(\Delta\phi)}{\partial x} = -\frac{j_0}{\sigma_m} \approx 0 \quad \in \{\partial\Omega_1 | x = 0\} \times (0, t), \tag{32}$$

$$\frac{\partial(\Delta\phi)}{\partial x} = \frac{j_0}{\sigma_s} \quad \in \{\partial\Omega_1 | x = L_0\} \times (0, t), \tag{33}$$

$$\Delta\phi = U/2 \quad \in \{\partial\Omega_1 | x = L_0\} \times (0, t). \tag{34}$$

The simplified model includes one governing equation, one initial condition, and three boundary conditions, which can be solved with ease (some commercial software can be employed to solve the equations) [45]. In general, only one parameter of j_0 and U is specified. This simplified model holds true when $\sigma_{s0} \gg \sigma_s$ and $\sigma_m \gg \sigma_s$. The unknown variable is $\Delta\phi$, and the storage charge is proportional to $\Delta\phi$.

The simplified model is compared against the general model, and the mode is selected as potentiostatic charging with $U = 1$ V. The conductivity of the confined electrolyte is fixed as $\sigma_s = 0.05$ S m^{-1}. The conductivity of the bulk electrolyte is assumed to be same as the conductivity of the porous electrode. Moreover, the conductivity ratio is defined as $\sigma^* = \sigma_{s0}/\sigma_s = \sigma_m/\sigma_s$. In the simplified model, the conductivity ratio can be considered as $\sigma^* \to \infty$. Figure 9(a) shows the stored charge, Q_m, for different conductivity ratios, σ^*, indicating that the simplified model overpredicts charge Q_m. When $\sigma^* = 1$, the discrepancy between the simplified model and the general model is obvious. These two models become consistent when $\sigma^* = 10$. The characteristic time, t_c, denotes the charging speed. Figure 9(b) illustrates the characteristic time, t_c, for different σ^*. Consequently, the simplified model is acceptable when σ^* is larger than ten.

VI. CONCLUDING REMARKS

In this study, a mathematical model that enables the dynamic processing of supercapacitor charging is developed. Three different charging modes, namely, potentiostatic charging, potentiodynamic charging, and galvanostatic charging, are discussed. For potentiostatic charging, the current is significant at the beginning and gradually decays to zero. The potential and current in the electrode and in the electrolyte can eventually achieve their steady states. For potentiodynamic and galvanostatic charging, the potential and current in an electrolyte can achieve their steady states. However, the potential in the electrode and the stored charge increase continuously, and no steady states are observed. This numerical model can be used to study the effect of parameters on the performance of supercapacitors and impedance spectroscopy. The results indicate that the conductivity of the electrolyte is the bottleneck that limits the charging rate of a supercapacitor, in particular, in thick electrode films. This mathematical model provides a powerful tool for optimizing the

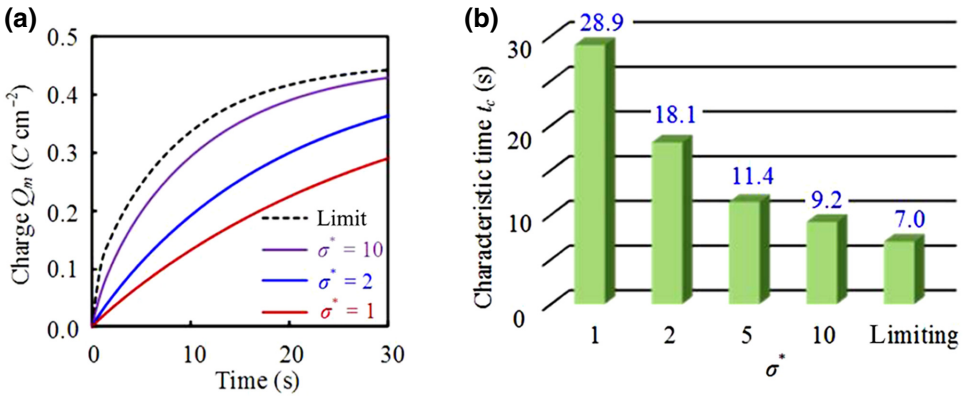

FIG. 9. Comparison between the general case and limiting case. (a) Stored charge, Q_m, for different conductivity ratios, σ^*. (b) Characteristic time, t_c, for different conductivity ratios, σ^*.

design of electrodes and electrolytes for high-performance supercapacitors.

ACKNOWLEDGMENTS

We acknowledge financial support by the National Natural Science Foundation of China (Grants No. 52175547, No. U21A20337, No. 52025055 and No. 51975467), the Natural Science Basic Research Program of Shaanxi (Grant No. 2022JQ-548), the Key Research and Development Program of Shaanxi (Grant No. 2021GY-294), and the Zhejiang Provincial Natural Science Foundation of China (Grant No. LQ21E050009).

The authors report no conflict of interest.

APPENDIX: DETAILS OF THE NUMERICAL SCHEME

The governing equations for the charging process are as follows:

$$\begin{aligned}
\frac{\partial^2\phi_m}{\partial x^2} &= \frac{AC_d}{\sigma_m}\frac{\partial(\phi_m-\phi_s)}{\partial t} \quad \in \Omega_1,\\
\frac{\partial^2\phi_s}{\partial x^2} &= -\frac{AC_d}{\sigma_s}\frac{\partial(\phi_m-\phi_s)}{\partial t} \quad \in \Omega_1,\\
\frac{\partial^2\phi_{s0}}{\partial x^2} &= 0 \quad \in \Omega_2,
\end{aligned} \tag{A1}$$

where ϕ_m, ϕ_s, and ϕ_{s0} represent the electric potential in the porous electrode, the confined electrolyte, and the bulk electrolyte, respectively; σ_m and σ_s denote the conductivity of the porous electrode and the confined electrolyte, respectively; A is the specific interfacial area of the porous electrode; and C_d denotes the specific differential capacitance of the electric double layer.

To solve the governing equations numerically, the computational domain is discretized (Fig. 10). The electrode is discretized into N_0 nodal points, and the separator is discretized into N_1 nodal points. The electric potential on the nodal points of the porous electrode, the confined electrolyte, and the bulk electrolyte can be denoted by $[\phi_{m,1}, \phi_{m,2}\ldots, \phi_{m,N_0}]$, $[\phi_{s,1}, \phi_{s,2}, \ldots, \phi_{s,N_0}]$, and $[\phi_{s0,1}, \phi_{s0,2}, \ldots, \phi_{s0,N_1}]$, respectively. In total, we have $2N_0+N_1$ unknowns to solve. If j_0 and U are further considered as two unknowns, then the total number of unknowns is $2N_0+N_1+2$. Governing Eq. (A1) at time $t+\Delta t$ can be discretized as follows:

$$\begin{aligned}
&\frac{\phi_{m,i+1}^{t+\Delta t}+\phi_{m,i-1}^{t+\Delta t}-2\phi_{m,i}^{t+\Delta t}}{\Delta x^2}\\
&\quad=\frac{AC_d}{\sigma_m}\left(\frac{\phi_{m,i}^{t+\Delta t}-\phi_{s,i}^{t+\Delta t}}{\Delta t}-\frac{\phi_{m,i}^{t}-\phi_{s,i}^{t}}{\Delta t}\right),\\
&\frac{\phi_{s,i+1}^{t+\Delta t}+\phi_{s,i-1}^{t+\Delta t}-2\phi_{s,i}^{t+\Delta t}}{\Delta x^2}\\
&\quad=\frac{AC_d}{\sigma_s}\left(\frac{\phi_{s,i}^{t+\Delta t}-\phi_{m,i}^{t+\Delta t}}{\Delta t}-\frac{\phi_{s,i}^{t}-\phi_{m,i}^{t}}{\Delta t}\right),\\
&\frac{\phi_{s0,i+1}^{t+\Delta t}+\phi_{s0,i-1}^{t+\Delta t}-2\phi_{s0,i}^{t+\Delta t}}{\Delta x^2}=0,
\end{aligned} \tag{A2}$$

which can be rewritten as

$$\begin{aligned}
&\phi_{m,i-1}^{t+\Delta t}-(2+a_1)\phi_{m,i}^{t+\Delta t}+\phi_{m,i+1}^{t+\Delta t}+a_1\phi_{s,i}^{t+\Delta t}\\
&\quad=-a_1(\phi_{m,i}^{t}-\phi_{s,i}^{t}),\\
&a_2\phi_{m,i}^{t+\Delta t}+\phi_{s,i-1}^{t+\Delta t}-(2+a_2)\phi_{s,i}^{t+\Delta t}+\phi_{s,i+1}^{t+\Delta t}\\
&\quad=-a_2(\phi_{s,i}^{t}-\phi_{m,i}^{t}),\\
&\phi_{s0,i-1}^{t+\Delta t}-2\phi_{s0,i}^{t+\Delta t}+\phi_{s0,i+1}^{t+\Delta t}=0,
\end{aligned} \tag{A3}$$

where $a_1\equiv AC_d\Delta x^2/\sigma_m\Delta t$, $a_2\equiv AC_d\Delta x^2/\sigma_s\Delta t$, Δx is the grid step, subscript i denotes the ith nodal point in the x direction, superscript t indicates the variable at time t, and Δt is the time step. Notably, in the first two equations of (A3), $2\le i\le N_0-1$. In the third equation of (A3), $2\le i\le N_1-1$. So far, we have $2N_0+N_1-6$ equations.

The next step is to discretize the boundary conditions. At the left boundary of the electrode, the current density of the electrolyte is zero: $j_s=-\sigma_s(\partial\phi_s/\partial x)=0$. Moreover, the current density of the porous matrix is expressed as $j_m=-\sigma_m(\partial\phi_m/\partial x)=j_0$. The electric potential of the porous matrix is specified, $\phi_m=U/2$. At the right boundary of the electrode, the current density of the porous matrix is zero, $j_m=-\sigma_m(\partial\phi_m/\partial x)=0$. In the domain of the bulk electrolyte, the electric potential at the middle plane is zero, $\phi_{s0}=0$. At the interface of the electrode and bulk electrolyte, the potential and current are continuous, $\phi_s=\phi_{s0}$ and $\sigma_s(\partial\phi_s/\partial x)=\sigma_{s0}(\partial\phi_{s0}/\partial x)$.

Combined with the governing equations, these boundary conditions can be rewritten in the discretized form. At the

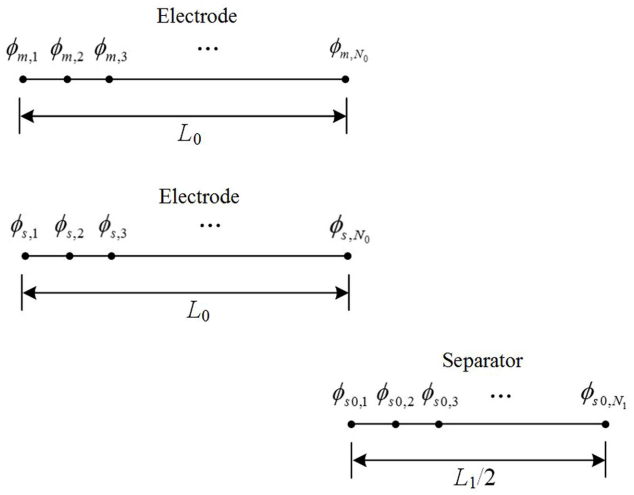

FIG. 10. Discretization of the computational domain.

left boundary of the electrode:

$$a_2\phi_{m,1}^{t+\Delta t} - (2+a_2)\phi_{s,1}^{t+\Delta t} + 2\phi_{s,2}^{t+\Delta t} = -a_2(\phi_{s,1}^{t} - \phi_{m,1}^{t}), \tag{A4}$$

$$-(2+a_1)\phi_{m,1}^{t+\Delta t} + 2\phi_{m,2}^{t+\Delta t} + a_1\phi_{s,1}^{t+\Delta t} + 2\frac{\Delta x}{\sigma_m}j_0 = -a_1(\phi_{m,1}^{t} - \phi_{s,1}^{t}), \tag{A5}$$

$$\phi_{m,1}^{t+\Delta t} - \frac{1}{2}U = 0. \tag{A6}$$

At the right boundary of the electrode, namely the interface of the electrode and bulk electrolyte:

$$2\phi_{m,N_0-1}^{t+\Delta t} - (2+a_1)\phi_{m,N_0}^{t+\Delta t} + a_1\phi_{s,N_0}^{t+\Delta t} = -a_1(\phi_{m,N_0}^{t} - \phi_{s,N_0}^{t}), \tag{A7}$$

$$\phi_{s,N_0}^{t+\Delta t} - \phi_{s0,1}^{t+\Delta t} = 0, \tag{A8}$$

$$a_2\phi_{m,N_0}^{t+\Delta t} + 2\phi_{s,N_0-1}^{t+\Delta t} - (2+a_2)\phi_{s,N_0}^{t+\Delta t} - 2\frac{\sigma_{s0}}{\sigma_s}\phi_{s0,1}^{t+\Delta t} + 2\frac{\sigma_{s0}}{\sigma_s}\phi_{s0,2}^{t+\Delta t} = -a_2(\phi_{s,N_0}^{t} - \phi_{m,N_0}^{t}). \tag{A9}$$

At the right boundary of the electrolyte:

$$\phi_{s0,N_1}^{t+\Delta t} = 0. \tag{A10}$$

Notably, for Eqs. (A4), (A5), (A7), and (A9), the boundary conditions are combined with the governing equations.

So far, we have $2N_0+N_1+1$ equations. One more boundary condition is required. In general, j_0 or U is specified during the charging process. For potentiostatic and potentiodynamic charging, the external voltage, U, is represented as follows:

$$U = U_{\text{const}}.$$

For galvanostatic charging, the current flux, j_0, is specified as follows:

$$j_0 = j_{\text{const}}.$$

So far, we have $2N_0+N_1+2$ equations.

The abovementioned equations can be written in the matrix form:

$$M\mathbf{X} = \mathbf{F}, \tag{A11}$$

where M is the global stiffness matrix, $\mathbf{X} = [\phi_{m,1}^{t+\Delta t}, \ldots, \phi_{m,N_0}^{t+\Delta t}, \phi_{s,1}^{t+\Delta t}, \ldots, \phi_{s,N_0}^{t+\Delta t}, \phi_{s0,1}^{t+\Delta t}, \ldots, \phi_{s0,N_1}^{t+\Delta t}, j_0, U]^T$ is the unknown vector, and $\mathbf{F}$ is the force vector. The expression of the force vector is $\mathbf{F} = [b_1, b_2, \ldots, b_{N0}, c_1, c_2, \ldots, c_{N0}, d_1, d_2, \ldots, d_{N1}, 0, e]^T$, where $b_i = -a_1(\phi_{m,i}^{t} - \phi_{s,i}^{t})$, $c_i = -a_2(\phi_{s,i}^{t} - \phi_{m,i}^{t})$, and $d_i = 0$. If the charging current is specified, then $e = j_{\text{const}}$. If the charging potential is specified, then $e = U_{\text{const}}$. The expression of matrix M is

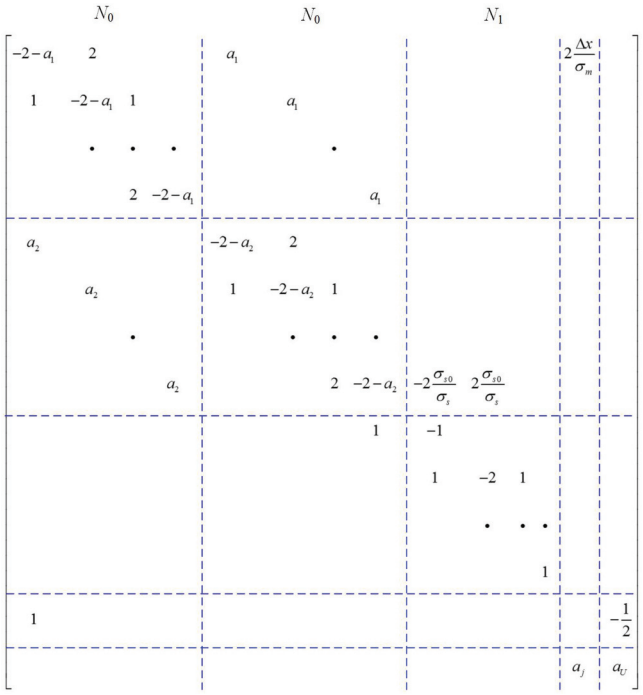

where $a_1 \equiv AC_d\Delta x^2/\sigma_m\Delta t$ and $a_2 \equiv AC_d\Delta x^2/\sigma_s\Delta t$ are previously defined. If the charging current is specified, then $a_j = 1$ and $a_U = 0$. If the charging potential is specified, then $a_j = 0$ and $a_U = 1$. With the initial conditions, the matrix can be solved in a time-marching manner and the unknowns at different times can be obtained. After solving ϕ_m, ϕ_s, and ϕ_{s0}, the charge densities q_m and q_s can be obtained.

[1] L. L. Zhang, R. Zhou, and X. Zhao, Graphene-based materials as supercapacitor electrodes, J. Mater. Chem. **20**, 5983 (2010).

[2] C. Liu, Z. Yu, D. Neff, A. Zhamu, and B. Z. Jang, Graphene-based supercapacitor with an ultrahigh energy density, Nano Lett. **10**, 4863 (2010).

[3] S. Kondrat, P. Wu, R. Qiao, and A. A. Kornyshev, Accelerating charging dynamics in subnanometre pores, Nat. Mater. **13**, 387 (2014).

[4] E. Frackowiak, Carbon materials for supercapacitor application, Phys. Chem. Chem. Phys. **9**, 1174 (2007).

[5] Y. Wang, Z. Shi, Y. Huang, Y. Ma, C. Wang, M. Chen, and Y. Chen, Supercapacitor devices based on graphene materials, J. Phys. Chem. C **113**, 13103 (2009).

[6] L. L. Zhang and X. Zhao, Carbon-based materials as supercapacitor electrodes, Chem. Soc. Rev. **38**, 2520 (2009).

[7] M. Salanne, B. Rotenberg, K. Naoi, K. Kaneko, P.-L. Taberna, C. P. Grey, B. Dunn, and P. Simon, Efficient storage mechanisms for building better supercapacitors, Nat. Energy **1**, 16070 (2016).

[8] X. Li, J. Shao, S.-K. Kim, C. Yao, J. Wang, Y.-R. Miao, Q. Zheng, P. Sun, R. Zhang, and P. V. Braun, High energy flexible supercapacitors formed via bottom-up infilling of gel electrolytes into thick porous electrodes, Nat. Commun. **9**, 2578 (2018).

[9] C. Zhong, Y. Deng, W. Hu, J. Qiao, L. Zhang, and J. Zhang, A review of electrolyte materials and compositions for electrochemical supercapacitors, Chem. Soc. Rev. **44**, 7484 (2015).

[10] F. Béguin, V. Presser, A. Balducci, and E. Frackowiak, Carbons and electrolytes for advanced supercapacitors, Adv. Mater. **26**, 2219 (2014).

[11] A. C. Forse, C. Merlet, J. M. Griffin, and C. P. Grey, New perspectives on the charging mechanisms of supercapacitors, J. Am. Chem. Soc. **138**, 5731 (2016).

[12] C. Péan, C. Merlet, B. Rotenberg, P. A. Madden, P.-L. Taberna, B. Daffos, M. Salanne, and P. Simon, On the dynamics of charging in nanoporous carbon-based supercapacitors, ACS Nano **8**, 1576 (2014).

[13] C. Merlet, B. Rotenberg, P. A. Madden, P.-L. Taberna, P. Simon, Y. Gogotsi, and M. Salanne, On the molecular origin of supercapacitance in nanoporous carbon electrodes, Nat. Mater. **11**, 306 (2012).

[14] L. Yang, B. H. Fishbine, A. Migliori, and L. R. Pratt, Molecular simulation of electric double-layer capacitors based on carbon nanotube forests, J. Am. Chem. Soc. **131**, 12373 (2009).

[15] M. Tokmachev and N. Tikhonov, Simulation of capacitive deionization accounting the change of stern layer thickness, J. Math. Chem. **57**, 2169 (2019).

[16] A. A. Kornyshev, Double-layer in ionic liquids: Paradigm change?, J. Phys. Chem. B **117**, 13946 (2013).

[17] Q. Zheng and G.-W. Wei, Poisson–boltzmann–nernst–Planck model, J. Chem. Phys. **134**, 194101 (2011).

[18] J. Varghese, H. Wang, and L. Pilon, Simulating electric double layer capacitance of mesoporous electrodes with cylindrical pores, J. Electrochem. Soc. **158**, A1106 (2011).

[19] H. Wang, J. Varghese, and L. Pilon, Simulation of electric double layer capacitors with mesoporous electrodes: Effects of morphology and electrolyte permittivity, Electrochim. Acta **56**, 6189 (2011).

[20] A. A. Kornyshev, The simplest model of charge storage in single file metallic nanopores, Faraday Discuss. **164**, 117 (2013).

[21] S. Kondrat and A. Kornyshev, Charging dynamics and optimization of nanoporous supercapacitors, J. Phys. Chem. C **117**, 12399 (2013).

[22] M. W. Verbrugge and P. Liu, Microstructural analysis and mathematical modeling of electric double-layer supercapacitors, J. Electrochem. Soc. **152**, D79 (2005).

[23] S. Kazaryan, S. Razumov, S. Litvinenko, G. Kharisov, and V. Kogan, Mathematical model of heterogeneous electrochemical capacitors and calculation of their parameters, J. Electrochem. Soc. **153**, A1655 (2006).

[24] R. Reddy and R. G. Reddy, Analytical solution for the voltage distribution in one-dimensional porous electrode subjected to cyclic voltammetric (CV) conditions, Electrochim. Acta **53**, 575 (2007).

[25] K. Somasundaram, E. Birgersson, and A. S. Mujumdar, Analysis of a model for an electrochemical capacitor, J. Electrochem. Soc. **158**, A1220 (2011).

[26] J. A. Staser and J. W. Weidner, Mathematical modeling of hybrid asymmetric electrochemical capacitors, J. Electrochem. Soc. **161**, E3267 (2014).

[27] F. Posey and T. Morozumi, Theory of potentiostatic and galvanostatic charging of the double layer in porous electrodes, J. Electrochem. Soc. **113**, 176 (1966).

[28] V. Srinivasan and J. W. Weidner, Mathematical modeling of electrochemical capacitors, J. Electrochem. Soc. **146**, 1650 (1999).

[29] H. Kim and B. N. Popov, A mathematical model of oxide/carbon composite electrode for supercapacitors, J. Electrochem. Soc. **150**, A1153 (2003).

[30] C. Lin, J. A. Ritter, B. N. Popov, and R. E. White, A mathematical model of an electrochemical capacitor with double-layer and faradaic processes, J. Electrochem. Soc. **146**, 3168 (1999).

[31] G. Sikha, R. E. White, and B. N. Popov, A mathematical model for a lithium-ion battery/electrochemical capacitor hybrid system, J. Electrochem. Soc. **152**, A1682 (2005).

[32] C. Lian, M. Janssen, H. Liu, and R. van Roij, Blessing and Curse: How a Supercapacitor's Large Capacitance Causes its Slow Charging, Phys. Rev. Lett. **124**, 076001 (2020).

[33] C. Péan, B. Rotenberg, P. Simon, and M. Salanne, Multi-scale modelling of supercapacitors: From molecular simulations to a transmission line model, J. Power Sources **326**, 680 (2016).

[34] O. Zikanov, *Essential Computational Fluid Dynamics* (John Wiley & Sons, Hoboken, New Jersey, 2010).

[35] T. Centeno and F. Stoeckli, The assessment of surface areas in porous carbons by two model-independent techniques, the DR equation and DFT, Carbon **48**, 2478 (2010).

[36] L. R. Faulkner and A. J. Bard, *Electrochemical Methods: Fundamentals and Applications* (John Wiley and Sons, cc, 2002).

[37] R. Lin, P.-L. Taberna, J. Chmiola, D. Guay, Y. Gogotsi, and P. Simon, Microelectrode study of pore size, ion size, and solvent effects on the charge/discharge behavior of microporous carbons for electrical double-layer capacitors, J. Electrochem. Soc. **156**, A7 (2008).

[38] A. C. Forse, J. M. Griffin, C. Merlet, J. Carretero-Gonzalez, A.-R. O. Raji, N. M. Trease, and C. P. Grey, Direct observation of ion dynamics in supercapacitor electrodes using in situ diffusion NMR spectroscopy, Nat. Energy **2**, 16216 (2017).

[39] R. Yuksel, O. Buyukcakir, P. K. Panda, S. H. Lee, Y. Jiang, D. Singh, S. Hansen, R. Adelung, Y. K. Mishra, and R. Ahuja, Necklace-like nitrogen-doped tubular carbon 3D frameworks for electrochemical energy storage, Adv. Funct. Mater. **30**, 1909725 (2020).

[40] P. Taberna, P. Simon, and J.-F. Fauvarque, Electrochemical characteristics and impedance spectroscopy studies of carbon-carbon supercapacitors, J. Electrochem. Soc. **150**, A292 (2003).

[41] P.-L. Taberna, C. Portet, and P. Simon, Electrode surface treatment and electrochemical impedance spectroscopy study on carbon/carbon supercapacitors, Appl. Phys. A **82**, 639 (2006).

[42] S. Buller, E. Karden, D. Kok, and R. De Doncker, Modeling the dynamic behavior of supercapacitors using impedance spectroscopy, IEEE Trans. Ind. Appl. **38**, 1622 (2002).

[43] Q. Zheng, X. Li, Q. Yang, C. Li, L. Wu, Y. Wang, P. Sun, H. Tian, C. Wang, and X. Chen, Compact 3D metal collectors enabled by roll-to-roll nanoimprinting for improving capacitive energy storage, Small Methods **6**, 2101539 (2022).

[44] Q. Zheng, X. Li, Q. Yang, C. Li, G. Liu, Y. Wang, P. Sun, H. Tian, C. Wang, and X. Chen, High performance solid-state supercapacitors based on highly conductive organogel electrolyte at low temperature, J. Power Sources **524**, 231102 (2022).

[45] G. Madabattula and S. Kumar, Insights into charge-redistribution in double layer capacitors, J. Electrochem. Soc. **165**, A636 (2018).